ADVANCED MATERIALS
www.advmat.de

Hole Transport Layer-Free Low-Bandgap Perovskite Solar Cells for Efficient All-Perovskite Tandems

Tianshu Ma, Huayang Wang, Zhanghao Wu, Yue Zhao, Cong Chen, Xinxing Yin, Lin Hu, Fang Yao, Qianqian Lin, Shaojun Wang, Dewei Zhao,* Xiaofeng Li,* and Changlei Wang**

Low-bandgap (LBG, E_g ≈1.25 eV) tin-lead (Sn-Pb) perovskite solar cells (PSCs) play critical roles in constructing efficient all-perovskite tandem solar cells (TSCs) that can surpass the efficiency limit of single-junction solar cells. However, the traditional poly(3,4-ethylenedioxythiophene):poly(styrenesulfonate) (PEDOT:PSS) hole transport layer (HTL) in LBG PSCs usually restricts device efficiency and stability. Here, a strategy of employing 2-aminoethanesulfonic acid (i.e., taurine) as the interface bridge to fabricate efficient HTL-free LBG PSCs with improved optoelectronic properties of the perovskite absorbers at the buried contacts is reported. Taurine-modified ITO substrate has lower optical losses, better energy level alignment, and higher charge transfer capability than PEDOT:PSS HTL, leading to significantly improved open-circuit voltage (V_{OC}) and short-circuit current density of corresponding devices. The best-performing LBG PSC with a power conversion efficiency (PCE) of 22.50% and an impressive V_{OC} of 0.911 V is realized, enabling all-perovskite TSCs with an efficiency of 26.03%. The taurine-based HTL-free TSCs have highly increased stability, retaining more than 90% and 80% of their initial PCEs after constant operation under 1-sun illumination for 600 h and under 55 °C thermal stress for 950 h, respectively. This work provides a facile strategy for fabricating efficient and stable perovskite devices with a simplified HTL-free architecture.

1. Introduction

Organic–inorganic hybrid perovskite solar cells (PSCs) are considered as one of the most promising photovoltaic technologies due to their high efficiency and low-cost solution processability. In recent years, the best power conversion efficiency (PCE) of single-junction PSCs has been boosted to 26%.[1,2] Perovskite-based tandem solar cells (TSCs) have garnered significant attention for their potential to achieve higher efficiencies, surpassing the Shockley–Queisser (S–Q) radiative limit of single-junction solar cells.[3–5] All-perovskite TSC typically comprises a low-bandgap (LBG, E_g ≈1.2–1.3 eV) mixed tin-lead (Sn-Pb) bottom subcell and a wide-bandgap (WBG, E_g ≈1.7–1.9 eV) top subcell, which reduces thermalization losses and maximizes sunlight utilization compared to single-junction photovoltaics.[6–8] The reported efficiency of all-perovskite TSCs has quickly increased to 28.5%[2,9] over the past 5 years. However, the performance of the

T. Ma, H. Wang, Z. Wu, Y. Zhao, S. Wang, X. Li, C. Wang
School of Optoelectronic Science and Engineering & Collaborative Innovation Center of Suzhou Nano Science and Technology
Key Lab of Advanced Optical Manufacturing Technologies of Jiangsu Province & Key Lab of Modern Optical Technologies of Education Ministry of China
Soochow University
Suzhou 215006, China
E-mail: swang.opto@suda.edu.cn; xfli@suda.edu.cn; cl.wang@suda.edu.cn

C. Chen, D. Zhao
College of Materials Science and Engineering & Institute of New Energy and Low-Carbon Technology
Engineering Research Center of Alternative Energy Materials & Devices Ministry of Education
Sichuan University
Chengdu 610065, China
E-mail: dewei_zhao@hotmail.com

X. Yin, L. Hu
China-Australia Institute for Advanced Materials and Manufacturing (IAMM)
Jiaxing University
Jiaxing 314001, China

F. Yao, Q. Lin
Key Laboratory of Artificial Micro- and Nano-Structures of Ministry of Education of China
School of Physics and Technology
Wuhan University
Wuhan 430072, China

The ORCID identification number(s) for the author(s) of this article can be found under https://doi.org/10.1002/adma.202308240

DOI: 10.1002/adma.202308240

state-of-the-art all-perovskite TSCs is still far away from the predicted values, partially ascribed to the inferior efficiency and stability of LBG Sn-Pb PSCs.[10–12]

Numerous strategies have been proposed to enhance the performance of LBG Sn-Pb PSCs, including the reducing agent additives and post-treatments. Tin fluoride (SnF_2), 4-trifluoromethylphenylammonium (CF3-PA), and other agents have been added into the precursor to suppress the oxidization of Sn^{2+} and reduce the internal vacancy defects.[13–17] Moreover, surface defects are detrimental to the device performance.[18–20] To address surface defects on the LBG perovskite film, maltol, and ethylene diammonium diiodide ($EDAI_2$) were utilized for passivating the surface and regulating surface potential, effectively increasing the short-circuit current density (J_{SC}) and open-circuit voltage (V_{OC}) of corresponding devices.[21,22]

Until now, only a few works have explored alternative hole transporting materials (HTMs) or constructed hole transporting layer (HTL)-free LBG PSCs,[23,24] as most efficient devices have been fabricated on traditional poly(3, 4-ethylenedioxythiophene):polystyrenesulfonate (PEDOT:PSS). However, PEDOT:PSS has acidic nature and hygroscopic properties, which detrimentally affect device stability. Efforts have been devoted on the finding of new materials replacing PEDOT:PSS. Kapil et al. reported hole transport bilayer with (2-(9H-carbazol-9-yl) ethyl) phosphonic acid (2PACz) and methyl phosphonic acid (MPA) in LBG PSCs, and achieved the highest PCE of 23.3% due to better energy level alignment and passivated buried interface.[23] Yu et al. employed low-temperature atomic layer deposition (ALD)-processed SnO_{2-x} and solution-processed SnOCl as the HTLs in LBG PSCs and all-perovskite TSCs, obtaining decent efficiencies and improved stability.[25,26] Recently, self-assembled monolayer (SAM) with an anchoring site and a dangling terminal has been proven to be effective HTLs in inverted PSCs. Brønsted–Lowry acids, such as phosphonic acid ($-P(=O)(OH)_2$),[27] and sulfonic acid ($-S(=O)(OH)_2$),[28] are the most reported anchoring sites of SAMs. Zhu et al. reported a donor–acceptor type molecule of MPA2FPh-BT-BA as a universal HTL in both WBG and LBG PSCs, leading to efficient all-perovskite TSCs.[29] Nevertheless, rare works have been reported on HTL-free LBG PSCs, especially all-perovskite TSCs. Therefore, it is highly desired to develop HTL-free PSCs with stable interfaces, reduced optical losses, and fluent charge selection to further boost the performance of LBG PSCs and all-perovskite TSCs.[25,30,31]

Herein, we selected a Brønsted–Lowry acid, i.e., 2-aminoethanesulfonic acid (taurine), to modulate the buried interface of LBG PSCs. Because taurine molecule has no conjugation backbone, it presents no charge selection capability when anchored on the conductive substrate, forming an HTL-free device architecture. The taurine layer has excellent optoelectronic properties, leading to improved J_{SC}s and V_{OC}s in corresponding PSCs. Meanwhile, taurine-modified ITO exhibits well-matched energy levels with the Sn-Pb perovskite film, reducing interfacial recombination and facilitating hole extraction in LBG PSCs. Finally, the taurine-based HTL-free LBG PSCs achieved a PCE of 22.50% with an impressive V_{OC} of 0.911 V. This enables us to fabricate all-perovskite TSCs with efficiencies of 26.03% and excellent stability, retaining more than 90% and 80% of their initial PCE of 600 h 1-sun illumination and 950 h of exposure to 55 °C thermal stress, respectively.

2. Results and Discussion

We selected the commonly used SAM material of (2-(3,6-dimethoxy-9H-carbazol-9-yl)ethyl)phosphonic acid (MeO-2PACz)[32] as the HTL to fabricate PEDOT:PSS-free LBG (1.25 eV $(FASnI_3)_{0.6}(MAPbI_3)_{0.4}$) PSCs. The SAM-based LBG PSCs show highly improved V_{OC}s compared the PEDOT:PSS-based ones (Figure S1, Supporting Information). However, it sacrifices the J_{SC}s and FFs dramatically, which might be caused to the poor film coverage and inhomogeneous surface morphology (Figures S2–S4, Supporting Information). We then selected a Brønsted–Lowry acid, i.e., taurine, to modulate the buried interface of LBG PSCs, and found it highly improved the performance of LBG PSCs. The special molecule structure of taurine is shown in **Figure 1**a with amino and sulfonic groups located at two ends. The sulfonic group anchors on the ITO substrates to form a self-assembled layer, while the amino terminal interacts with the following perovskite layer.

We then fabricated LBG films on different substrates to investigate their optoelectronic properties, including bare ITO, taurine-modulated ITO (hereafter referred to as taurine), and PEDOT:PSS substrates. Figure S5 (Supporting Information) shows the cross-sectional scanning electron microscope (SEM) images of LBG PSCs fabricated on various substrates. It is clear that the taurine layer is too thin to be distinguished, while the PEDOT:PSS HTL presents a thickness about 30 nm.

We suppose that the strong electrostatic effect and electric dipole of taurine layer significantly promote the carrier transfer from perovskite layer to ITO substrates, which can compensate the moderate hole extraction capability of taurine with no conjugation backbone. We further investigate the surface work functions of ITO, taurine, and PEDOT:PSS via Kelvin probe force microscope (KPFM) measurement (Figure S6, Supporting Information), and the corresponding energy levels are shown in Figure 1b. The bare ITO has a work function of −4.70 eV, while the taurine-coated ITO has a downward shifted work function of −5.26 eV, even deeper than PEDOT:PSS of −5.15 eV, demonstrating a better energy level alignment with the LBG perovskite layer.[33] The well-matched energy levels are undoubtedly beneficial to increase the V_{OC}s of corresponding PSCs due to a large built-in potential and low voltage loss at the buried perovskite interface.

The photoluminescence (PL) spectra and transient PL (TRPL) decays of different films are shown in Figure 1c,d. The taurine sample has the lowest PL intensity, which might be caused by the most efficient charge extraction at the buried interface. The TRPL results further confirm the improved charge transfer dynamics in taurine sample with the averaged carrier lifetime of 145 ns, much shorter than those of the ITO (461 ns) and PEDOT:PSS (378 ns) analogues.

We also studied the crystallinity of perovskite films grown on different substrates by X-ray diffraction (XRD) measurement (Figure 1e). All samples show strong (110) and (220) diffraction peaks, indicating highly preferred orientation. Taurine sample has the highest peak intensity and smallest full-with-half-maximum (FWHM) value of (110) peak (Figure S7, Supporting

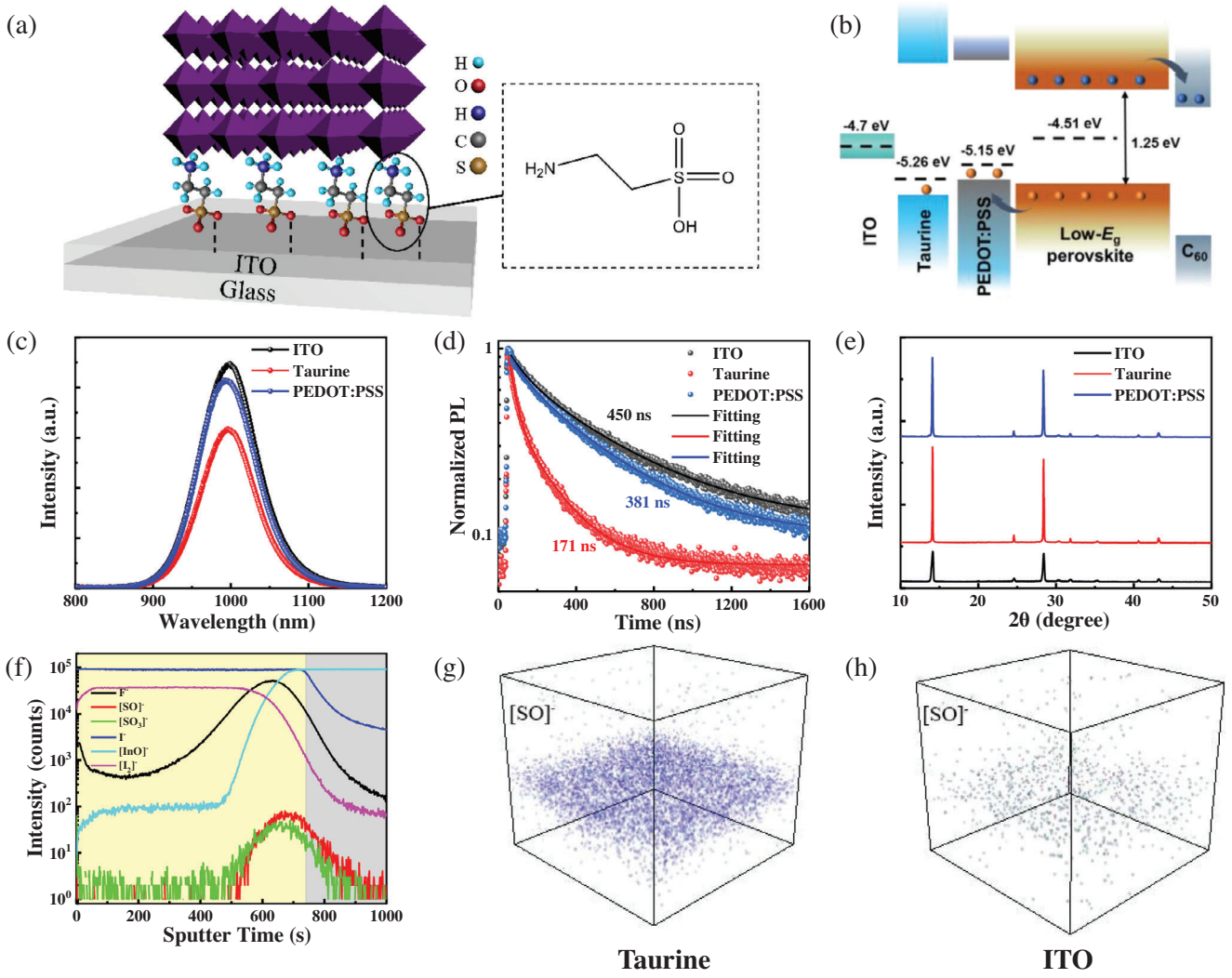

Figure 1. Optoelectronic and compositional properties of perovskite films on different substrates. a) Schematic diagram of taurine structure anchored on the substrate. b) Energy level diagrams of bare ITO, taurine, and PEDOT:PSS with LBG perovskite film. c) Steady-state PL, d) TRPL results, and e) XRD patterns of perovskite films based on ITO, taurine modified ITO, and PEDOT:PSS. f,g) ToF-SIMS profiles of anion distribution for perovskite films on taurine or ITO.

Information), demonstrating the best crystallinity. While the ITO-based film shows the worst crystallinity, implying bare ITO is not suitable for the growth of high-quality LBG perovskite films.

Taurine has no conjugation backbone; therefore, we suppose that the taurine layer cannot be very thick to get rid of the charge accumulation at the substrate/perovskite interface. We optimized the concentration of taurine at 10 mg mL^{-1} (Figures S8 and S9, Supporting Information). Taurine layer was first deposited on the ITO substrate, followed by annealing at 100 °C for 5 min, and then the LBG perovskite precursor was deposited on the taurine modified substrate through spin-coating. This process will wash out the un-anchored molecules from the ITO substrate, because the excessive taurine will be dissolved by the mixture of *N, N*-dimethylformamide (DMF) and dimethyl sulfoxide (DMSO) solvents (Figure S10, Supporting Information). We further tested the thickness of the anchored taurine layer on ITO after washing with the mixed DMF/DMSO solvent using atomic force microscope (AFM). The thickness of the anchored taurine layer is ≈3 nm (Figure S11, Supporting Information). We then probed the distribution of taurine via time-of-flight secondary ion mass spectrometry (ToF-SIMS), as shown in Figure 1f. For taurine sample, the element profiles of the SO_3^- and SO^- species are located mainly at the buried interface of perovskite film, confirming the presence of taurine, i.e., taurine is not totally washed away after perovskite layer deposition. In contrast, the control film has very weak signal of sulfur elements. The tiny amount of sulfur might be caused by the contamination of ITO substrates from the ambient condition. ToF-SIMS depth profiles for perovskite film on bare ITO, as well as the 3D spatial distribution maps of sulfur and other elements for both samples are shown in Figures S12–S14 (Supporting Information), further confirming the successful interface bonding and modification of taurine on ITO.

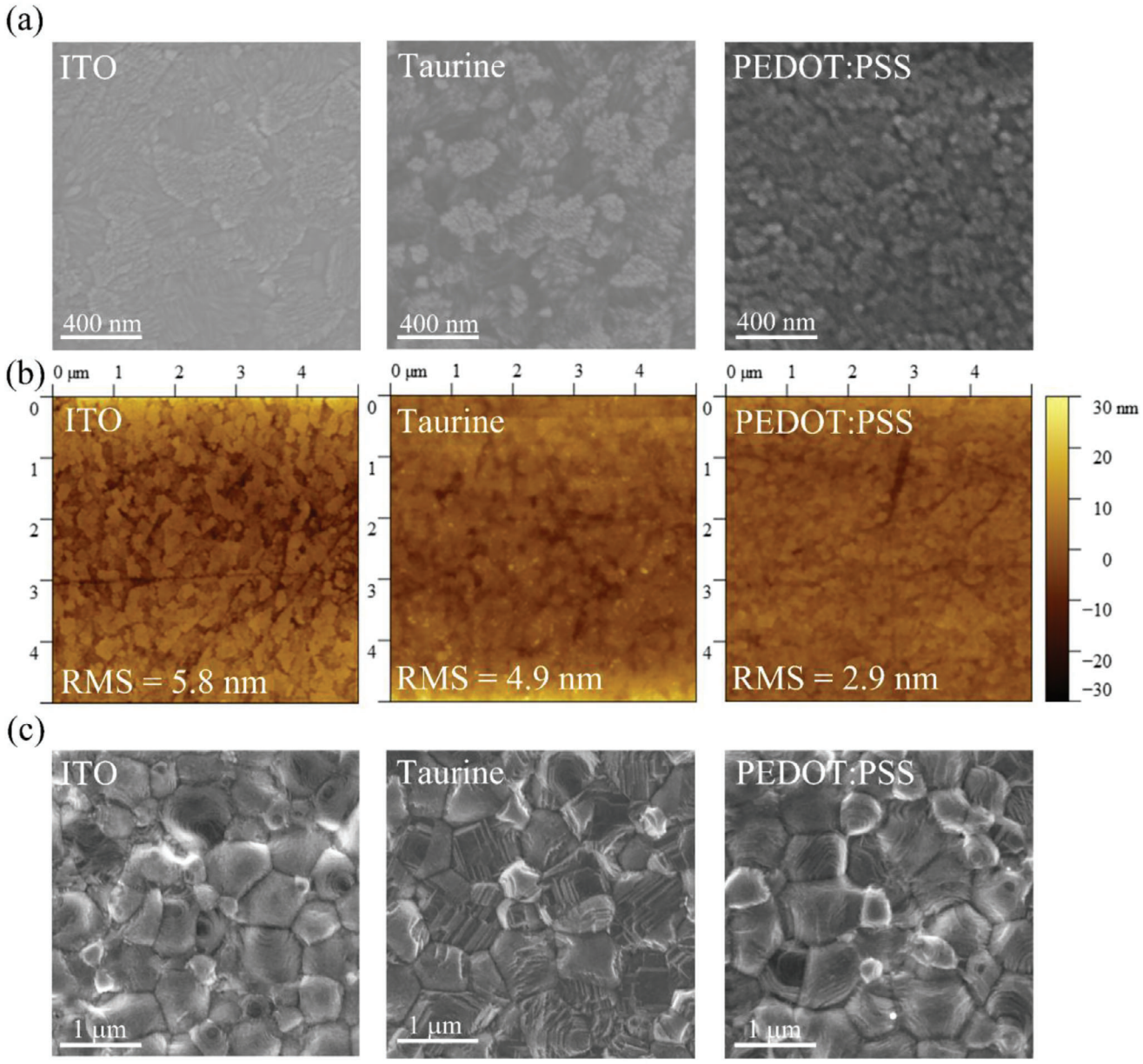

Figure 2. Surface morphology of different substrates and perovskite films. a) Top-view SEM images and b) AFM images of ITO, taurine/ITO, and PEDOT:PSS/ITO. c) Top-view SEM images of perovskite films on three different substrates.

We further investigated the film quality and topological uniformity of various substrates and consequent perovskite layers via SEM and AFM measurements, as shown in **Figure 2**. Bare ITO substrate shows a rough surface with small ITO particles, and the corresponding root mean square (RMS) value is 5.8 nm (Figure 2a,b). The taurine layer shows similar surface topology compared to ITO substrate; however, the surface roughness of taurine-modified ITO substrate decreases to 4.9 nm, which should be ascribed to the filling effect of taurine molecules locating at the deep valleys of bare ITO substrates. The PEDOT:PSS layer shows a hazy surface morphology compared to ITO and taurine, which we attribute to the large thickness with relatively lower carrier conductivity. The surface roughness of PEDOT:PSS is further reduced to 2.9 nm, demonstrating the thick layer of PEDOT:PSS has completely covered the surface structure of ITO substrate. We scrutinize the hydrophobicity of different substrates through contact angle measurement of DMF solvent (Figure S15, Supporting Information). The contact angles are 11.4°, 10.6°, and 8.5° for bare ITO, taurine/ITO, and PEDOT:PSS/ITO layers, respectively. All samples show small contact angles, implying better wettability of these substrates, facilitating the deposition of high-quality perovskite films.[34]

Figure 2c shows the SEM images of LBG perovskite films fabricated on three substrates. They show similar surface morphology with clear texture, which can be related to the domain crystallization mode with preferred orientation, consistent with

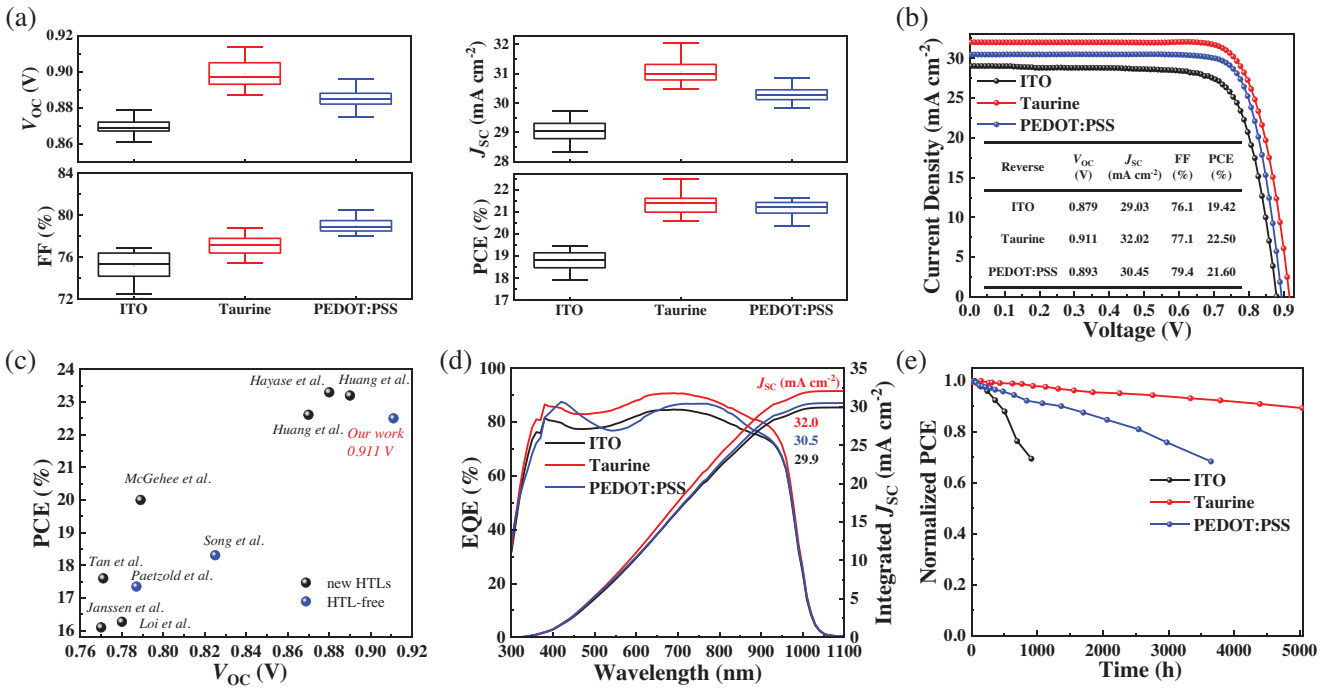

Figure 3. Performance of LBG PSCs with different substrates. a) Statistics of V_{OC}, J_{SC}, FF, and PCE of PSCs on various substrates. Each parameter was calculated from 50 individual cells. b) J–V curves under reverse scan of PSCs on different substrates. c) Summary on PCEs and V_{OC}s of LBG PSCs without PEDOT:PSS HTLs. d) EQE spectra of PSCs on different substrates and their EQE-integrated J_{SC}s. e) PCE evolution of encapsulated devices stored in the glovebox.

the aforementioned XRD results.[35–37] Perovskite film grown on bare ITO shows inhomogeneous surface with relatively small grain size and large roughness, while the other films on taurine and PEDOT:PSS have bigger grain size over 1 µm. Moreover, compared to PEDOT:PSS, perovskite film on taurine presents a more pronounced stripe topological feature, indicating taurine can facilitate the growth of perovskite grains with higher crystallinity and domain morphology (Figure 1e). The RMS roughness is 45.0, 39.5, and 38.0 nm for films on ITO, taurine, and PEDOT:PSS, respectively (Figure S16, Supporting Information). The lower roughness indicates a smooth and flat perovskite surface, which enables a better contact quality at the back interface with electron transport layers (ETLs).

We fabricated numerous LBG PSCs on three substrates, and the statistical results of photovoltaic parameters are shown in **Figure 3**a. PSCs on bare ITO have the worst performance due to the severe nonradiative charge recombination at the buried interface, while after the introduction of taurine or PEDOT:PSS, the device efficiency has been significantly enhanced. The averaged V_{OC} of taurine-based PSC reaches 0.898 ± 0.007 V, much larger than those of the other devices on bare ITO or PEDOT:PSS, which should be ascribed to the lower Fermi level of taurine, leading to a larger built-in potential in the corresponding devices. Moreover, the averaged J_{SC} of taurine-modified PSCs achieves 31.07 ± 0.36 mA cm^{-2}, also higher than that of 30.28 ± 0.22 mA cm^{-2} for the PEDOT:PSS analogue. Taurine enables the enhancement of V_{OC} and J_{SC} compared to PEDOT:PSS, however, it sacrifices the FF. We suppose the moderate FF values of taurine-modified PSCs are related to the insufficient charge extraction at the buried interface due to the lacking of conjugation backbone in taurine molecule.

The J–V curves of the best-performing PSCs fabricated on different substrates are displayed in Figure 3b. Bare ITO PSC shows the lowest PCE of 19.42%, with a V_{OC} of 0.879 V, a J_{SC} of 29.03 mA cm^{-2}, and an FF of 76.1%. While PEDOT:PSS PSC has a relatively higher PCE of 21.60%, with a V_{OC} of 0.893 V, a J_{SC} of 30.45 mA cm^{-2}, and an FF of 79.4%. Taurine PSC exhibits the best PCE of 22.50% with a V_{OC} of 0.911 V, a J_{SC} of 32.02 mA cm^{-2}, and an FF of 77.1%. To the best of our knowledge, the impressive V_{OC} of 0.911 V is the highest value among the LBG PSCs without PEDOT:PSS HTLs (Figure 3c).[23–26,30,38–42] Figure S17 (Supporting Information) shows the hysteresis of the devices with different substrates. Taurine and PEDOT:PSS-based PSCs have negligible hysteresis, indicating the fluent and balanced charge transfer inside the cells.

To analyze the increase in the J_{SC} upon taurine modulation, we measured the EQE curves of various PSCs. As shown in Figure 3d, the taurine PSC shows the highest spectra response at the whole wavelength region than the others, indicating the negligible optical losses and the efficient light harvesting, which finally results in the integrated J_{SC} of 32.0 mA cm^{-2}. The integrated J_{SC}s are 29.9 and 30.5 mA cm^{-2} for bare ITO and PEDOT:PSS-based PSCs, respectively, consistent with the J_{SC} values obtained from J–V curves. It is worth noticing that PEDOT:PSS-based PSC has an obvious deep valley in the EQE spectrum at the wavelength around 550 nm, which is likely caused by the huge difference of refractive index between ITO and PEDOT:PSS.

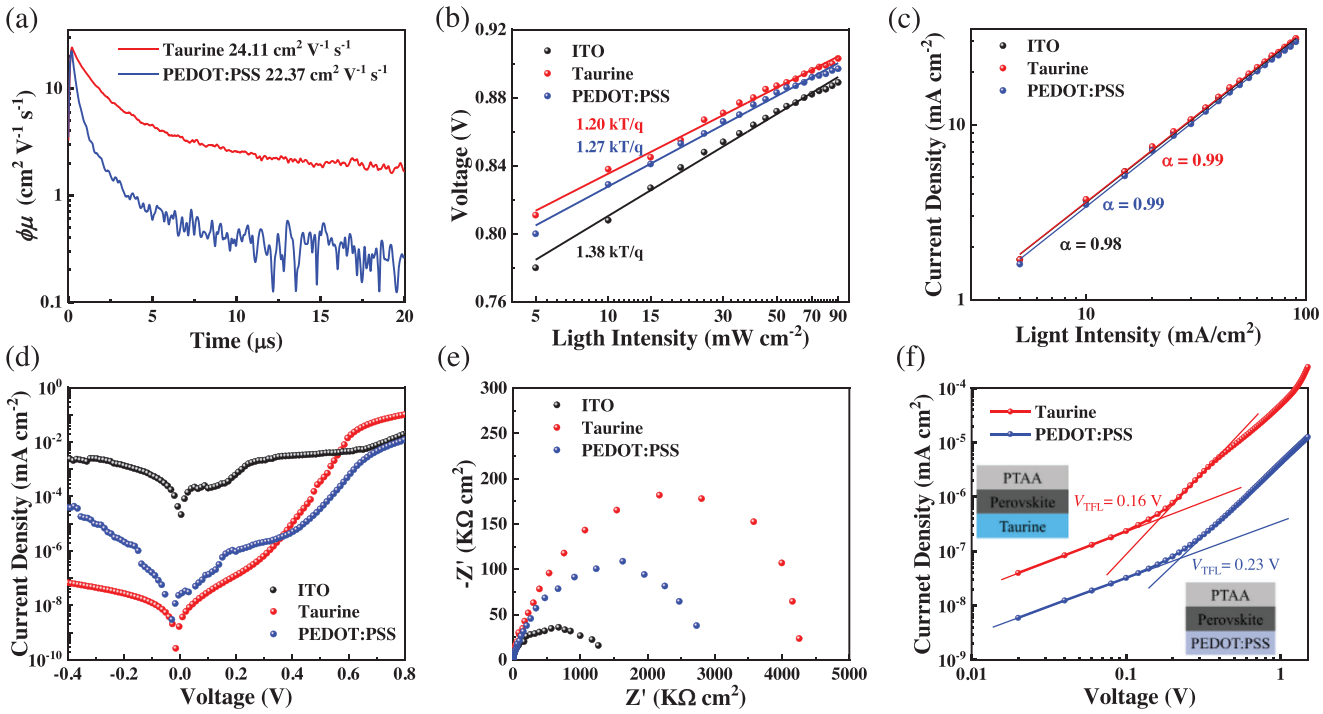

Figure 4. Carrier dynamic characteristics of LBG PSCs. a) TRMC curves of perovskite films based on taurine and PEDOT:PSS substrates. b) V_{OC} and c) J_{SC} as a function of light intensity. d) Dark *J*–*V* curves and e) Nyquist plots of the devices with ITO, taurine, and PEDOT:PSS substrates. f) *J*–*V* curves of hole-only devices on different substrates based on SCLC protocol.

We further carried out the transmittance and reflectance measurements of various substrates and perovskite films. Figure S18 (Supporting Information) shows the optical properties of the substrates. We can find that PEDOT:PSS itself has the highest transmittance and lowest reflectance. However, when deposited with LBG perovskite films, the PEDOT:PSS sample presents the largest reflectance loss, as displayed in Figure S19 (Supporting Information). In the wavelength range of 500–800 nm, the reflectance of perovskite film on PEDOT:PSS substrate (>10%) is larger than that on ITO and taurine substrates, consistent with the EQE results. We attribute the severe optical loss mainly to the reflection. In order to further verify our conclusion, we carried out optical simulation of perovskite films on different substrates upon the multiphysics-modeling software. Figure S20 (Supporting Information) shows simulated absorption and reflectance spectra of perovskite films on ITO and PEDOT:PSS substrates. We find the PEDOT:PSS significantly decreases the perovskite film absorption due to the increased refection in the range of 430–800 nm.

We then tested long-term storage stability of encapsulated devices under a N_2 atmosphere, as shown in Figure 3e. The ITO device quickly decreases to 68% of the initial PCE in the first 1000 h, while PEDOT:PSS device declines to 68% of the original PCE for 3700 h. Taurine-based device shows the best stability by keeping 90% of initial PCE after storage for 5000 h.

To further study the charge carrier dynamics in Sn–Pb perovskite films, we carried out time-resolved microwave conductivity (TRMC) measurements (Note S1, Supporting Information). **Figure 4**a shows the decay curves of perovskite films fabricated on taurine and PEDOT:PSS substrates. Both samples showed similar charge carrier mobility-yield product ($\phi\mu$) of 24.12 and 22.37 $cm^2\ V^{-1}\ s^{-1}$, respectively. The slightly higher $\phi\mu$ of taurine sample indicates the improved charge transport properties.[43,44] More importantly, the charge carrier mobility increased significantly, which is beneficial for increasing the charge carrier concentration at open-circuit conduction, which could result enhanced V_{OC} within the devices.[45,46]

We then measured the light intensity dependence of V_{OC} and J_{SC} of different PSCs, as shown in Figure 4b,c. The diode ideal factor (n) values are 1.38, 1.27, and 1.20 for ITO, PEDOT:PSS, and taurine-based device, respectively, which supports a gradual increase in n due to the reduced nonradiative Shockley–Read–Hall (SRH) recombination (Figure 4b).[47] Figure 4c shows the dependence of J_{SC} on the light intensity, and J_{SC} has a linear relation with light intensity according to $J_{sc} \propto I^{\alpha}$. All three samples have similar slope approaching 1, indicating the small space charge limited current in all of our LBG PSCs.

The dark currents were recorded by measuring the *J*–*V* curves of the PSCs in dark (Figure 4d). PSCs on PEDOT:PSS and taurine have much lower dark currents than bare ITO, suggesting the suppressed current leakage and the reduced charge recombination loss, which ensures the relatively higher V_{OC} and FF of corresponding PSCs. The lowest dark current of taurine device represents the smallest saturation current density due to the highly improved film quality with good crystallinity and low defects as discussed above. Figure 4e displays the Nyquist plots of PSCs by electrochemical impedance spectroscopy (EIS) measurements. Previous reports have proposed that the semicircle at low frequency is related to the recombination resistance (R_{rec}).[48] We extracted the recombination resistance of 1.17×10^5, 3.85×10^5,

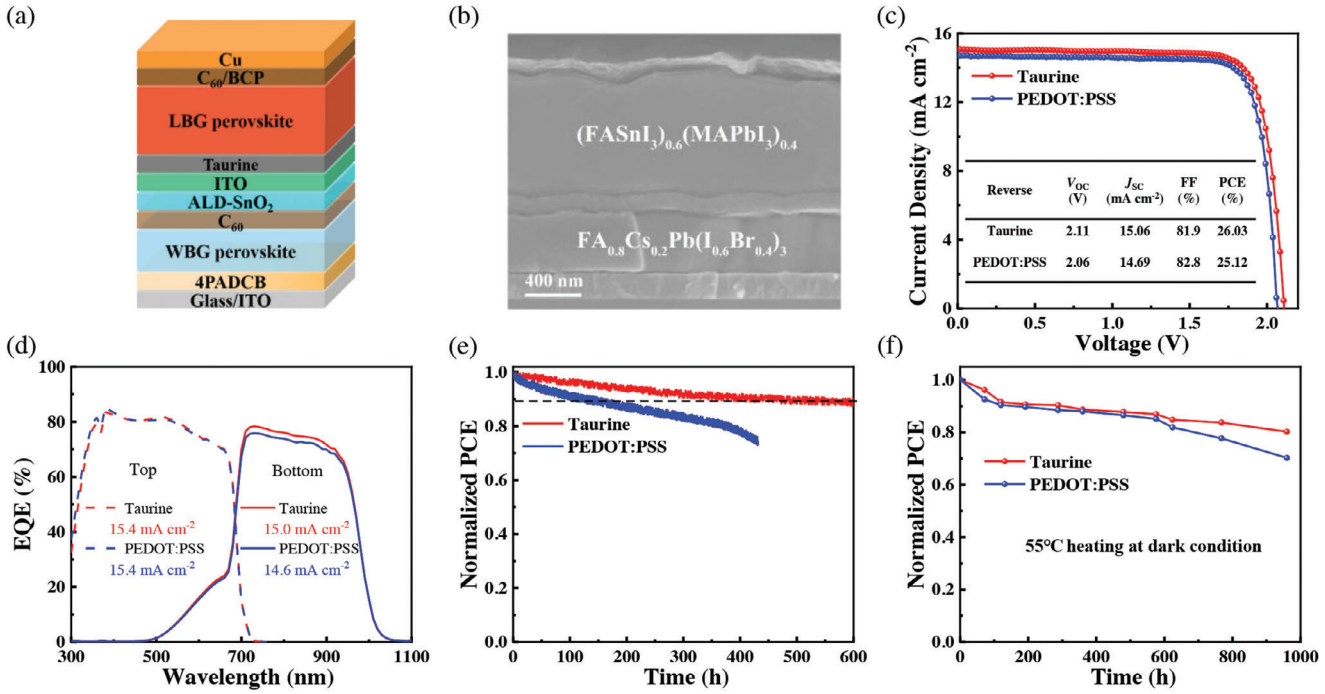

Figure 5. Performance of all-perovskite TSCs with different ICLs. a) Device structure and b) cross-sectional SEM image of one taurine-based all-perovskite TSC. c) Champion *J*–*V* curves and d) EQE curves of TSCs with taurine and PEDOT:PSS ICLs. e) Constant power output of encapsulated TSCs using different interconnection layers under simulated 1-sun illumination. f) Long-term thermal stability for all-perovskite TSCs using PEDOT:PSS or taurine interconnection layers under a thermal stress at 55 °C for 950 h.

and 2.63×10^5 Ω for ITO, taurine and PEDOT:PSS devices, respectively, by fitting the equivalent circuit (Figure S21, Supporting Information). Taurine device has the largest radius of the semicircle in the Nyquist plot, demonstrating the lowest charge recombination due to the reduced defects and well aligned energy levels.

To clearly recognize the reduced trap density of the perovskite film with taurine layer, we measured the space charge limited current (SCLC) of the hole-only devices, as shown in Figure 4f. The trap density in perovskite films was calculated following the equation of $V_{TFL} = qN_{trap}L^2/(2\varepsilon_r\varepsilon_0)$, where V_{TFL} is trap-filled limit voltage, q is the electron charge, L is the thickness of perovskite film, ε_r is the relative dielectric constant of perovskite, and ε_0 is the vacuum permittivity. The V_{TFL} of PEDOT:PSS and taurine devices are 0.23 and 0.16 V, respectively, leading to the corresponding trap density of 1.8×10^{15} and 1.3×10^{15} cm^{-3}.[47,49,50] The lower trap density in taurine device implies the significantly suppressed defects at the interface of taurine/perovskite.

We fabricated monolithic all-perovskite TSCs using the optimized LBG perovskite layers paired with WBG subcells (**Figure 5**a,b). The 1.77 eV $FA_{0.8}Cs_{0.2}Pb(I_{0.6}Br_{0.4})_3$ WBG PSC exhibits a PCE of 18.02%, with a V_{OC} of 1.28 V, a J_{SC} of 17.33 mA cm^{-2}, and an FF of 81.4% (Figure S22, Supporting Information). The LBG bottom subcells were deposited on ITO/ALD SnO_2/C_{60} interconnection layers (ICLs), and the AFM images of ITO on glass and SnO_2/C_{60}/WBG sample are shown in Figure S23 (Supporting Information). The champion taurine-based TSC achieves the highest PCE of 26.03% under reverse voltage scan, with a V_{OC} of 2.11 V, a J_{SC} of 15.06 mA cm^{-2}, and an FF of 81.9% (Figure 5c). While the TSC on PEDOT:PSS has an inferior PCE of 25.12%, with a V_{OC} of 2.06 V, a J_{SC} of 14.69 mA cm^{-2}, and an FF of 82.8%. Both devices have a negligible hysteresis under reverse and forward scans (Figure S24, Supporting Information). Figure 5d shows the EQE spectra of TSCs based on PEDOT:PSS and taurine ICLs. The taurine-based TSC has the integrated current densities of 15.4 and 15.0 mA cm^{-2} for the top and bottom subcells, respectively. While the PEDOT:PSS TSCs has a relatively lower current density of 14.6 mA cm^{-2} for bottom subcell compared to the taurine one, which might be caused by the inevitable parasitic absorption of PEDOT:PSS at long wavelength region, thus leading to the lower J_{SC} of corresponding TSCs.

We investigated the operating stability TSCs by maximum power point (MPP) tracking under 1-sun illumination with a light-emitting diode (LED) source with intensity equivalent to 100 mW cm^{-2} (Figure 5e). The encapsulated taurine TSC maintains 90% of the initial PCE after 600 h continuous operation, while the PEDOT:PSS-based TSC remains only 75% of the initial PCE after 400 h. In addition, we found the highest temperature of single-junction LBG PSCs during MPP tracking under constant 1 sun illumination can reach 55 °C without any cooling unit. Therefore, we further monitored the thermal stability of TSCs with different ICLs by recording the performance of encapsulated devices on a 55 °C hotplate by excluding the impact of illumination (Figure 5f). The taurine TSC remains 80% of its original efficiency after 950 h, while the PEDOT:PSS sample keeps only 70% of its initial efficiency after the same duration. The better stability of taurine-based TSCs can be ascribed to excellent optoelectronic properties of the taurine layer, and the high-quality LBG films with improved crystallinity, prolonged carrier diffusion length, reduced trap density and suppressed recombination.

3. Conclusion

We have developed efficient HTL-free LBG PSCs by incorporating taurine as the interface modification layer. The presence of taurine facilitates the growth of high-quality LBG perovskite films, resulting in improved crystallinity and domain morphology, thereby reducing defects and nonradiative recombination in PSCs. Additionally, the taurine layer exhibits superior optical and electronical properties compared to the traditional PEDOT:PSS HTL, leading to enhanced light absorption and charge transfer capability. As a result of these improvements, the single-junction LBG PSC achieves an impressive PCE of 22.50% with a remarkable V_{OC} of 0.911 V. This allows us to fabricate all-perovskite TSCs with the best PCE of 26.03%. Moreover, taurine-based TSCs have excellent operational and thermal stability that remained 90% and 80% of the initial PCEs under constant 1-sum illumination for 600 h and 55 °C thermal stress for 950 h, respectively. Our work presents a promising avenue to fabricate HTL-free LBG PSCs and all-perovskite TSCs, offering enhanced stability and efficiency in these photovoltaic devices.

Supporting Information

Supporting Information is available from the Wiley Online Library or from the author.

Acknowledgements

T.M. and H.W. contributed equally to this work. The work was financially supported by the National Key R&D Program of China (No. 2022YFB4200303), National Natural Science Foundation of China (Nos. 62005188, 62174112, 62275184, and 62120106001), Natural Science Foundation of Jiangsu Province (Nos. BK20190825 and BK20200859), Natural Science Research Project of Jiangsu Higher Education Institutions (No. 22KJA480003), Fundamental Research Funds for the Central Universities (No. YJ201955), Engineering Featured Team Fund of Sichuan University (No. 2020SCUNG102), the Tang Scholar.

Conflict of Interest

The authors declare no conflict of interest.

Data Availability Statement

The data that support the findings of this study are available from the corresponding author upon reasonable request.

Keywords

all-perovskite tandem solar cells, hole transport layer-free, low-bandgap tin-lead, perovskite solar cells, taurine

Received: August 14, 2023
Revised: November 14, 2023
Published online:

[1] A. Kojima, K. Teshima, Y. Shirai, T. Miyasaka, *J. Am. Chem. Soc.* **2009**, *131*, 6050.
[2] M. A. Green, E. D. Dunlop, G. Siefer, M. Yoshita, N. Kopidakis, K. Bothe, X. Hao, *Prog. Photovolt. Res. Appl.* **2023**, *31*, 3.
[3] W. Shockley, H. J. Queisser, *J. Appl. Phys.* **1961**, *32*, 510.
[4] S. Wang, P. Wang, B. Chen, R. Li, N. Ren, Y. Li, B. Shi, Q. Huang, Y. Zhao, M. Grätzel, X. Zhang, *eScience* **2022**, *2*, 339.
[5] C. Wang, Y. Zhao, T. Ma, Y. An, R. He, J. Zhu, C. Chen, S. Ren, F. Fu, D. Zhao, X. Li, *Nat. Energy* **2022**, *7*, 744.
[6] F. Lang, M. A. Gluba, S. Albrecht, J. Rappich, L. Korte, B. Rech, N. H. Nickel, *J. Phys. Chem. Lett.* **2015**, *6*, 2745.
[7] M. Jaysankar, B. A. L. Raul, J. Bastos, C. Burgess, C. Weijtens, M. Creatore, T. Aernouts, Y. Kuang, R. Gehlhaar, A. Hadipour, J. Poortmans, *ACS Energy Lett.* **2019**, *4*, 259.
[8] R. He, S. Ren, C. Chen, Z. Yi, Y. Luo, H. Lai, W. Wang, G. Zeng, X. Hao, Y. Wang, J. Zhang, C. Wang, L. Wu, F. Fu, D. Zhao, *Energy Environ. Sci.* **2021**, *14*, 5723.
[9] R. Lin, Y. Wang, Q. Lu, B. Tang, J. Li, H. Gao, Y. Gao, H. Li, C. Ding, J. Wen, P. Wu, C. Liu, S. Zhao, K. Xiao, Z. Liu, C. Ma, Y. Deng, L. Li, F. Fan, H. Tan, *Nature* **2023**, *620*, 994.
[10] D. Zhao, C. Chen, C. Wang, M. M. Junda, Z. Song, C. R. Grice, Y. Yu, C. Li, B. Subedi, N J. Podraza, X. Zhao, G. Fang, R.-G. Xiong, K. Zhu, Y. Yan, *Nat. Energy* **2018**, *3*, 1093.
[11] R. Lin, K. Xiao, Z. Qin, Q. Han, C. Zhang, M. Wei, M I. Saidaminov, Y. Gao, J. Xu, M. Xiao, A. Li, J. Zhu, E H. Sargent, H. Tan, *Nat. Energy* **2019**, *4*, 864.
[12] C. Li, Z. Song, C. Chen, C. Xiao, B. Subedi, S P. Harvey, N. Shrestha, K. K. Subedi, L. Chen, D. Liu, Y. Li, Y.-W. Kim, C.-S. Jiang, M J. Heben, D. Zhao, R J. Ellingson, N J. Podraza, M. Al-Jassim, Y. Yan, *Nat. Energy* **2020**, *5*, 768.
[13] L. Ma, F. Hao, C. C. Stoumpos, B. T. Phelan, M. R. Wasielewski, M. G. Kanatzidis, *J. Am. Chem. Soc.* **2016**, *138*, 14750.
[14] S. J. Lee, S. S. Shin, Y. C. Kim, D. Kim, T. K. Ahn, J. H. Noh, J. Seo, S. I. Seok, *J. Am. Chem. Soc.* **2016**, *138*, 3974.
[15] J. Tong, Z. Song, D. H. Kim, X. Chen, C. Chen, A. F. Palmstrom, P. F. Ndione, M. O. Reese, S. P. Dunfield, O. G. Reid, J. Liu, F. Zhang, S. P. Harvey, Z. Li, S. T. Christensen, G. Teeter, D. Zhao, M. M. Al-Jassim, M. F. A. M. Van Hest, M. C. Beard, S. E. Shaheen, J. J. Berry, Y. Yan, K. Zhu, *Science* **2019**, *364*, 475.
[16] K. Xiao, R. Lin, Q. Han, Y. Hou, Z. Qin, H. T. Nguyen, J. Wen, M. Wei, V. Yeddu, M. I. Saidaminov, Y. Gao, X. Luo, Y. Wang, H. Gao, C. Zhang, J. Xu, J. Zhu, E. H. Sargent, H. Tan, *Nat. Energy* **2020**, *5*, 870.
[17] R. Lin, J. Xu, M. Wei, Y. Wang, Z. Qin, Z. Liu, J. Wu, K. Xiao, B. Chen, S. M. Park, G. Chen, H. R. Atapattu, K. R. Graham, J. Xu, J. Zhu, L. Li, C. Zhang, E. H. Sargent, H. Tan, *Nature* **2022**, *603*, 73.
[18] Z. Fang, L. Jia, N. Yan, X. Jiang, X. Ren, S. Yang, S. Liu, *InfoMat* **2022**, *4*, e12307.
[19] L. Xie, X. Zhao, J. Wang, J. Li, C. Liu, S. Wang, Q. Bao, M. Yang, X. Niu, F. Hao, Z. Ge, *InfoMat* **2023**, *5*, e12379.
[20] Y. Liu, B. Dong, A. Hagfeldt, J. Luo, M. Graetzel, *SmartMat.* **2021**, *2*, 33.
[21] S. Hu, M. A. Truong, K. Otsuka, T. Handa, T. Yamada, R. Nishikubo, Y. Iwasaki, A. Saeki, R. Murdey, Y. Kanemitsu, A. Wakamiya, *Chem. Sci.* **2021**, *12*, 13513.
[22] S. Hu, K. Otsuka, R. Murdey, T. Nakamura, M. A. Truong, T. Yamada, T. Handa, K. Matsuda, K. Nakano, A. Sato, K. Marumoto, K. Tajima, Y. Kanemitsu, A. Wakamiya, *Energy Environ. Sci.* **2022**, *15*, 2096.
[23] G. Kapil, T. Bessho, Y. Sanehira, S. R. Sahamir, M. Chen, A. K. Baranwal, D. Liu, Y. Sono, D. Hirotani, D. Nomura, K. Nishimura, M. A. Kamarudin, Q. Shen, H. Segawa, S. Hayase, *ACS Energy Lett.* **2022**, *7*, 966.
[24] J. Wang, Z. Yu, D. D. Astridge, Z. Ni, L. Zhao, B. Chen, M. Wang, Y. Zhou, G. Yang, X. Dai, A. Sellinger, J. Huang, *ACS Energy Lett.* **2022**, *7*, 3353.
[25] Z. Yu, Z. Yang, Z. Ni, Y. Shao, B. Chen, Y. Lin, H. Wei, Z. J. Yu, Z. Holman, J. Huang, *Nat. Energy* **2020**, *5*, 657.

[26] Z. Yu, J. Wang, B. Chen, M. A. Uddin, Z. Ni, G. Yang, J. Huang, *Adv. Mater.* **2022**, *34*, 2205769.
[27] R. He, W. Wang, Z. Yi, F. Lang, C. Chen, J. Luo, J. Zhu, J. Thiesbrummel, S. Shah, K. Wei, Y. Luo, C. Wang, H. Lai, H. Huang, J. Zhou, B. Zou, X. Yin, S. Ren, X. Hao, L. Wu, J. Zhang, J. Zhang, M. Stolterfoht, F. Fu, W. Tang, D. Zhao, *Nature* **2023**, *618*, 80.
[28] F. Han, Z. Tu, Z. Wan, J. Luo, J. Xia, G. Hao, Y. Yi, R. Wang, C. Jia, *Appl. Surf. Sci.* **2018**, *462*, 517.
[29] J. Zhu, Y. Luo, R. He, C. Chen, Y. Wang, J. Luo, Z. Yi, J. Thiesbrummel, C. Wang, F. Lang, H. Lai, Y. Xu, J. Wang, Z. Zhang, W. Liang, G. Cui, S. Ren, X. Hao, H. Huang, Y. Wang, F. Yao, Q. Lin, L. Wu, J. Zhang, M. Stolterfoht, F. Fu, D. Zhao, *Nat. Energy* **2023**, *8*, 714.
[30] P. Gómez, J. Wang, M. Más-Montoya, D. Bautista, C. H. L. Weijtens, D. Curiel, R. A. J. Janssen, *Sol. RRL* **2021**, *5*, 2100454.
[31] N. Yaacobi-Gross, N. D. Treat, P. Pattanasattayavong, H. Faber, A. K. Perumal, N. Stingelin, D. D. C. Bradley, P. N. Stavrinou, M. Heeney, T. D. Anthopoulos, *Adv. Energy Mater.* **2015**, *5*, 1401529.
[32] A. Al-Ashouri, E. Köhnen, B. Li, A. Magomedov, H. Hempel, P. Caprioglio, J. A. Márquez, A. B. Morales Vilches, E. Kasparavicius, J. A. Smith, N. Phung, D. Menzel, M. Grischek, L. Kegelmann, D. Skroblin, C. Gollwitzer, T. Malinauskas, M. Jost, G. Matic, B. Rech, R. Schlatmann, M. Topic, L. Korte, A. Abate, B. Stannowski, D. Neher, M. Stolterfoht, T. Unold, V. Getautis, S. Albrecht, *Science* **2020**, *370*, 1300.
[33] H. Tang, Y. Shang, W. Zhou, Z. Peng, Z. Ning, *Sol. RRL* **2019**, *3*, 1800256.
[34] S. Zhang, F. Ye, X. Wang, R. Chen, H. Zhang, L. Zhan, X. Jiang, Y. Li, X. Ji, S. Liu, M. Yu, F. Yu, Y. Zhang, R. Wu, Z. Liu, Z. Ning, D. Neher, L. Han, Y. Lin, H. Tian, W. Chen, M. Stolterfoht, L. Zhang, W.-H. Zhu, Y. Wu, *Science* **2023**, *380*, 404.
[35] S. Seo, I. J. Park, M. Kim, S. Lee, C. Bae, H. S. Jung, N.-G. Park, J. Y. Kim, H. Shin, *Nanoscale* **2016**, *8*, 11403.
[36] X. Ren, Z. Yang, D. Yang, X. Zhang, D. Cui, Y. Liu, Q. Wei, H. Fan, S. (F.). Liu, *Nanoscale* **2016**, *8*, 3816.
[37] S. Wang, Z. Ma, B. Liu, W. Wu, Y. Zhu, R. Ma, C. Wang, *Sol. RRL* **2018**, *2*, 1800034.
[38] S. Shao, Y. Cui, H. Duim, X. Qiu, J. Dong, G. H. Ten Brink, G. Portale, R. C. Chiechi, S. Zhang, J. Hou, M. A. Loi, *Adv. Mater.* **2018**, *30*, 1803703.
[39] Q. Han, Y. Wei, R. Lin, Z. Fang, K. Xiao, X. Luo, S. Gu, J. Zhu, L. Ding, H. Tan, *Sci. Bull.* **2019**, *64*, 1399.
[40] J. Werner, T. Moot, T. A. Gossett, I. E. Gould, A. F. Palmstrom, E. J. Wolf, C. C. Boyd, M. F. A. M. Van Hest, J. M. Luther, J. J. Berry, M. D. Mcgehee, *ACS Energy Lett.* **2020**, *5*, 1215.
[41] F. Lv, Y. Yao, C. Xu, D. Liu, L. Liao, G. Wang, G. Zhou, X. Zhao, D. Liu, X. Yang, Q. Song, *ACS Appl. Mater. Interfaces* **2021**, *4*, 1294.
[42] S. Moghadamzadeh, I. M. Hossain, M. Loy, D. B. Ritzer, H. Hu, D. Hauschild, A. Mertens, J.-P. Becker, A. A. Haghighirad, E. Ahlswede, L. Weinhardt, U. Lemmer, B. A. Nejand, U. W. Paetzold, *ACS Appl. Mater. Interfaces* **2021**, *13*, 46488.
[43] H. Oga, A. Saeki, Y. Ogomi, S. Hayase, S. Seki, *J. Am. Chem. Soc.* **2014**, *136*, 13818.
[44] R. R. Prabhakar, T. Moehl, D. Friedrich, M. Kunst, S. Shukla, D. Adeleye, V. H. Damle, S. Siol, W. Cui, L. Gouda, J. Suh, Y. R. Tischler, R. van de Krol, S. D. Tilley, *Adv. Funct. Mater.* **2022**, *32*, 2112184.
[45] Q. Lin, Z. Wang, H. J. Snaith, M. B. Johnston, L. M. Herz, *Adv. Sci.* **2018**, *5*, 1700792.
[46] Y. Li, Z. Jia, Y. Yang, F. Yao, Y. Liu, Q. Lin, *Appl. Phys. Rev.* **2023**, *10*, 011406.
[47] J. Chen, N.-G. Park, *Adv. Mater.* **2019**, *31*, 1803019.
[48] R. Yuan, B. Cai, Y. Lv, X. Gao, J. Gu, Z. Fan, X. Liu, C. Yang, M. Liu, W.-H. Zhang, *Energy Environ. Sci.* **2021**, *14*, 5074.
[49] V. M. Le Corre, E. A. Duijnstee, O. El Tambouli, J. M. Ball, H. J. Snaith, J. Lim, L. J. A Koster, *ACS Energy Lett.* **2021**, *6*, 1087.
[50] T. Bu, X. Liu, Y. Zhou, J. Yi, X. Huang, L. Luo, J. Xiao, Z. Ku, Y. Peng, F. Huang, Y.-B. Cheng, J. Zhong, *Energy Environ. Sci.* **2017**, *10*, 2509.